ARTICLE   OPEN

Check for updates

Self-driven WSe$_2$ photodetectors enabled with asymmetrical van der Waals contact interfaces

Changjian Zhou [1✉], Shouyong Zhang[1], Zhe Lv[1], Zichao Ma[2], Cui Yu[3], Zhihong Feng[3✉] and Mansun Chan[2]

Self-driven photodetectors that can detect light without any external voltage bias are important for low-power applications, including future internet of things, wearable electronics, and flexible electronics. While two-dimensional (2D) materials exhibit good optoelectronic properties, the extraordinary properties have not been fully exploited to realize high-performance self-driven photodetectors. In this paper, a metal–semiconductor–metal (MSM) photodetector with graphene and Au as the two contacts have been proposed to realize the self-driven photodetector. Van der Waals contacts are formed by dry-transfer methods, which is important in constructing the asymmetrical MSM photodetector to avoid the Fermi-level pinning effect. By choosing graphene and Au as the two contact electrodes, a pronounced photovoltaic effect is obtained. Without any external bias, the self-driven photodetector exhibits a high responsivity of 7.55 A W^{-1} and an ultrahigh photocurrent-to-dark current ratio of ~10^8. The photodetector also shows gate-tunable characteristics due to the field-induced Fermi-level shift in the constituent 2D materials. What is more, the high linearity of the photodetector over almost 60 dB suggests the easy integration with processing circuits for practical applications.

INTRODUCTION

Photodetectors that convert the light information into electrical information have been widely utilized in photography[1], optical communication[2], and analytical instruments[3]. Currently, the silicon-based photodetector is the workhorse behind the commercial image sensors embedded in mobile phones and digital cameras[4–6]. However, the application of silicon photodiode in the infrared and ultraviolet spectrum is limited due to its low absorption coefficient or high dark current[7,8]. To utilize the full light spectrum targeting emerging application fields such as biological imaging[9], environment monitoring[10], and flexible photodetectors[11], emerging semiconductor materials and device structures are being assessed on their suitability for photodetector development[12,13]. The advent of two-dimensional (2D) materials has provided a tremendous amount of candidates covering almost all the interesting light spectrum for photodetectors exploration[14]. During the last decade, various photodetectors based on the 2D materials have been demonstrated with superior properties[15–18]. Early demonstrations used a back-gated field-effect transistor (FET) structure and the operational principle was mainly based on the photoconductive effect. The photodiodes are not readily obtained as reliable doping methods like ion-implantation are not suitable for 2D materials. Instead, local electrostatic gating by using a split gate has been proposed to realize a WSe$_2$ PN junction, and a pronounced photovoltaic (PV) effect has been obtained[19]. Alternatively, as different 2D materials exhibit different carrier polarity, combining different 2D materials could form the heterostructures with pronounced PV effect[20]. The main advantages of the PV effect-based photodetectors, including low dark current and small operating voltage, would enable a low-power or even self-driven photodetectors for applications in internet of things (IoT) and wearable electronics[21,22]. 2D material-based self-driven photodetectors have received intense research

efforts recently[23], and these photodetectors have exhibited superior performances in terms of responsivity, response time, and detectivity. However, in terms of low dark current and linearity, as critically commented in recent works[24,25], the 2D photodetectors are still much inferior to that of the commercial photodetectors.

In this paper, we designed an asymmetrical metal–semiconductor–metal (MSM) photodetector by using graphene and Au as the contacting electrodes to the WSe$_2$ flake. To avoid the notorious Fermi-level pinning effect, a dry-transfer method is adopted to construct the van der Waals contacts. An ultrahigh photocurrent-to-dark current ratio up to 10^8 is obtained at a zero bias. The self-driven photodetector also exhibits a gate-tunable PV effect thanks to the gate-tunable Fermi level of the 2D WSe$_2$ and graphene. The fabrication of the proposed device structure does not involve any external chemical doping or complex split gate structure, ensuring a stable and low-cost process for self-driven photodetectors.

RESULTS AND DISCUSSION

Device operational principle and fabrication process

Traditionally, the MSM structures are adopted for photodetectors due to the low dark current and also a simple planar fabrication process[7]. Figure 1a shows the band alignment of a traditional MSM photodetector with Au as the contact electrodes to WSe$_2$. The left panel shows the band diagram of Au and WSe$_2$ before contact. The valence band maximum (VBM) and conduction band minimum (CBM) is −5.18 and −4.03 eV, respectively[26], and the Fermi level of WSe$_2$ is located at the middle between the CBM and VBM, as confirmed by the ambipolar transfer curves of the WSe$_2$ FET. The work function of the Au and Gr is about 5.1 and 4.56 eV, respectively[27,28]. As the MSM photodetector can be modeled as
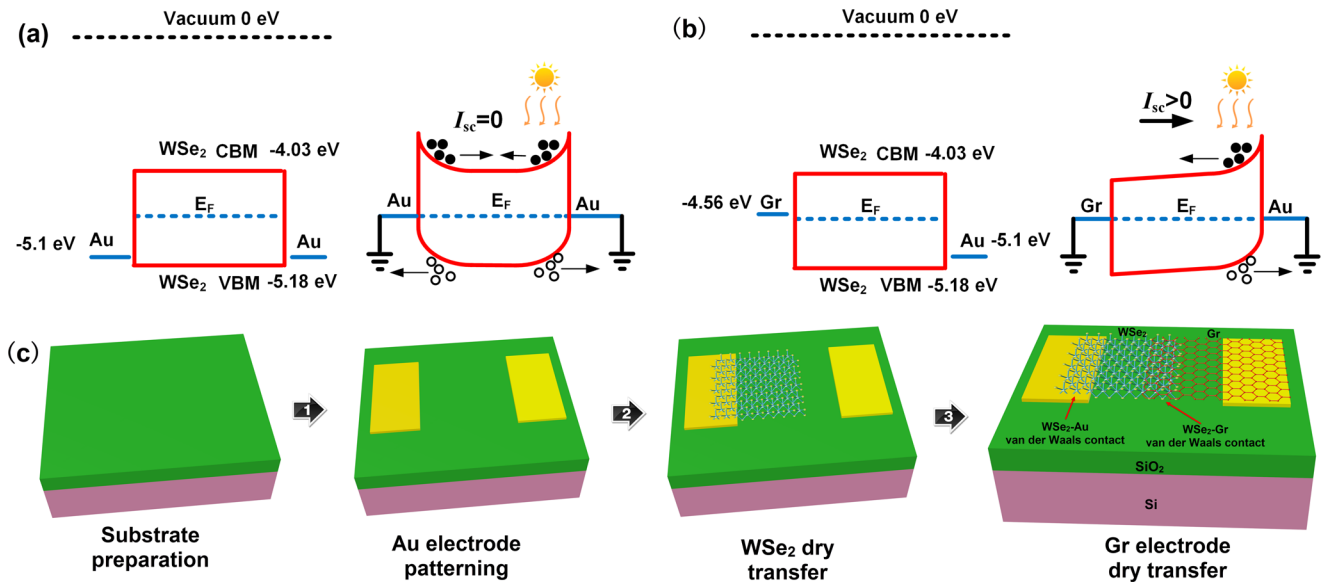
Fig. 1 Operational principle and the fabrication process of the photodetector. Band alignment of the Metal–WSe$_2$–Metal structures with **a** Au as the two contact electrodes and **b** Au and multilayer graphene as the two contact electrodes, respectively, where the asymmetrical Schottky barriers at the two sides enabling a non-zero short-circuit current under light illumination. **c** Three-dimensional schematic of the process flow to fabricate the graphene–WSe$_2$–Au photodetector.

two MS junctions connected back to back, the total current density under light illumination flows through the MSM photodetector is given by

$$J = J_L + J_R = \left[J_{SL}(e^{qV_L/\eta kT} - 1) + qGW_L \right]$$
$$- \left[J_{SR}(e^{-qV_R/\eta kT} - 1) + qGW_R \right], \quad (1)$$

where J_L (J_R) and J_{SL} (J_{SR}) are the current density and the reverse saturation current density of the MS junction at the left (right) side, respectively. V_L and V_R are the voltage applied to the left and right MS junction whose sum is determined by external bias voltage between the two electrodes $V_{ds} = V_L + V_R$. η is the ideality factor of the MS junction, and k is the Boltzmann constant. J_{SL} (J_{SR}) is dependent on the Richardson constant A^* and the Schottky barrier height Φ_{BL} (Φ_{BR}) as given by[7]

$$J_{SL} = A^* T^2 e^{-q\Phi_{BL}/kT}. \quad (2)$$

The thermionic emission theory predicts that the A^* is solely dependent on the semiconductor side, which is WSe$_2$ in this study. Thus for a symmetrical Au–WSe$_2$–Au photodetector, Φ_{BL} is equal to Φ_{BR}, resulting in an equal reverse saturation current at the two MS junctions. The second term in the expression of J_L (J_R) is contributed from the photogenerated current, and G and W_L (W_R) denotes the carrier generation rate and the depletion width at the left (right) MS junction. The depletion width W_L (W_R) is related to the external voltage bias:

$$W_L = \sqrt{2\varepsilon_s(V_{BL} + V_L)/qN_d}, \quad (3)$$

$$W_R = \sqrt{2\varepsilon_s(V_{BR} - V_R)/qN_d}, \quad (4)$$

where ε_s and N_d are the dielectric constant and carrier concentration of WSe$_2$, respectively. V_{BL} (V_{BR}) is the built-in potential of the MS junction at the left (right) side, which can be expressed as $V_{BL} = \Phi_{BL} - \Psi n$, where Ψn is the energy difference between the CBM and the Fermi level.

When the device is short circuited, both V_L and V_R are zero, and the total current is contributed by the difference in the second term, which gives $J = qG(W_L - W_R)$. As shown in the right panel of Fig. 1a, for the symmetrical Au–WSe$_2$–Au MSM photodetector, W_L

is equal to W_R at zero external bias voltage, which results in a zero short-circuit photocurrent (I_{sc}). In that case, a non-zero photocurrent can be induced by applying an external voltage which is mainly applied to the reverse-biased MS junction and causes a difference between W_L and W_R. Note that the semiconductor WSe$_2$ is the same throughout this study, and Ψn is the same for both the two MS junctions. Thus a large I_{sc} can be expected by forming two asymmetrical MS junctions with different barrier height. Figure 1b shows the energy band diagram of the asymmetrical graphene–WSe$_2$–Au MSM photodetector, which schematically illustrates that a large difference between W_L and W_R can be obtained even without any external bias, thanks to the intrinsic difference between Φ_{BL} and Φ_{BR}.

As the key to obtaining the self-driven photodetector is to ensure a large difference of barrier height for the two constituent MS junctions, one may choose two electrodes with different work functions to construct the asymmetrical MSM photodetectors. However, traditional metal deposition methods, including sputtering and evaporation, induce defects and Fermi level pinning at the interface[27], which makes it challenging to form asymmetrical MSM photodetectors with observable photovoltaic effects just by choosing two different metal materials. To address this problem, we adopted a PDMS-assisted dry-transfer method, as shown in Fig. 1c. The Au–WSe$_2$ MS junction is formed first by transferring a WSe$_2$ flake onto the pre-patterned Au electrodes, and the other constituent graphene–WSe$_2$ MS junction is formed by transferring a multilayer graphene flake onto the WSe$_2$ flake. In this way, both of the electrodes form a van der Waals contact with the WSe$_2$ flake, and the barrier height difference is highly dependent on the work function difference of the two electrode materials.

Electrical characteristics of the photodetector

Figure 2a illustrates the optical microscope image of a fabricated MSM photodetector with asymmetrical contact electrodes. The red dashed lines show the contact edges of the Au–WSe$_2$ and graphene–WSe$_2$ MS junctions. The effective area of WSe$_2$ in between the two electrodes is about 507.1 μm^2, as calculated from the optical image. The Raman spectrum measured on the graphene–WSe$_2$ contact area is presented in Fig. 2b. Both of the
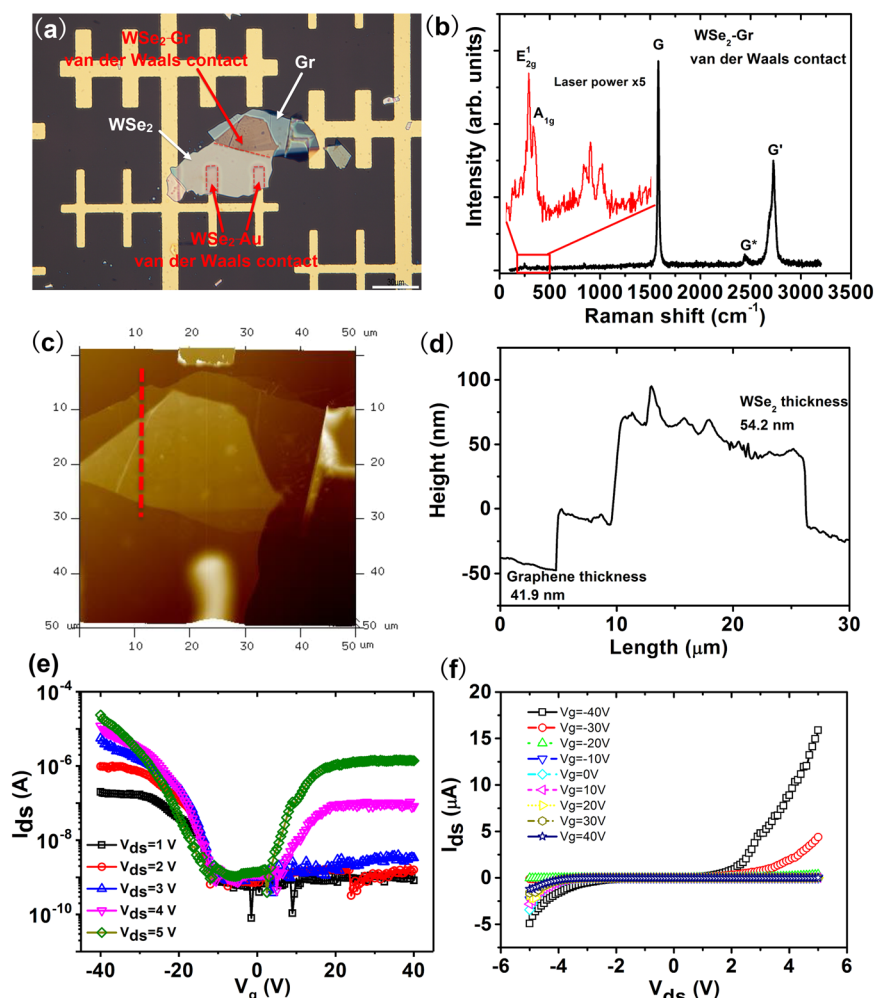
Fig. 2 Device fabrication and basic electrical characteristics. a Optical picture of one fabricated graphene–WSe$_2$–Au structure by the dry-transfer process. The red dashed lines indicate the boundary of the van der Waals contacts. Scale bar 30 μm. **b** Raman spectrum obtained on the multilayer graphene–WSe$_2$ contact region. For the lower Raman shift range, the laser power is increased to five times to identify the WSe$_2$ characteristics. The excitation wavelength is 532 nm. **c** Atomic force microscope image of the fabricated graphene–WSe$_2$–Au structure. **d** Height profile of the graphene–WSe$_2$ heterostructure along the red dashed line in **c**. **e** Transfer curves and **f** output curves of the fabricated graphene–WSe$_2$–Au structure.

G (1580.5 cm^{-1}) and G' (2726.6 cm^{-1}) peaks of graphene are observed, and the relatively weaker peaks at 247.9 and 256.6 cm^{-1} are corresponding to the E_{2g} and A_{1g} modes of multilayer WSe$_2$, respectively. Note that a much higher Raman laser power is applied to obtain the WSe$_2$ characteristics due to the graphene coated on top of the WSe$_2$. The Raman spectra obtained from the graphene and WSe$_2$ flakes near the overlapped region are presented in Supplementary Fig. 1a, b, which show the same peak positions but different intensities, especially for the WSe$_2$ flake. Raman peak shift is usually used as an indicator to access the strain effect or the quenching effect[29–31]. The experimental results suggest the lack of observable strain effect or quenching effects in the heterostructures. The low Raman intensity of WSe$_2$ is probably due to the relatively thick multilayer graphene on top of the WSe$_2$, which absorbs a lot of incoming light and reflected light from the WSe$_2$. The thicknesses of the WSe$_2$ and graphene flakes are measured by atomic force microscopy (AFM) method. Figure 2c shows the AFM image of the device highlighting the graphene–WSe$_2$ contact region, and the height profile along the red dashed line is presented in Fig. 2d, from which the graphene and WSe$_2$ thicknesses are extracted as 41.9 nm and 54.2 nm, respectively. Considering the high absorption coefficient of the 2D

material, the relatively thick WSe$_2$ flake could ensure a nearly total light absorption for optimal photodetector development.

Figure 2e shows the transfer curves of the fabricated device. The gate voltage is applied to the silicon back gate and the thermally grown 100 nm SiO$_2$ is used as the gate dielectric. The graphene–WSe$_2$–Au structure exhibits ambipolar transport properties. Note that the V_{ds} bias voltage is applied to the graphene electrode, and the Au electrode is set as the ground. When a small V_{ds} is applied ($V_{ds} = 1$ V), the device shows only hole transport, and electron transport is suppressed due to the large Schottky barrier between the Au and WSe$_2$. This feature is further identified by the output curves shown in Fig. 2f, which shows clearly non-linear asymmetrical I_{ds}–V_{ds} characteristics. The output curves imply that a large contact resistance is present due to the reverse-biased MS junction. In terms of normal FETs or photodetectors based on the photoconductive mechanism, a low-resistance Ohmic contact is desired. While for MSM photodetectors, a large Schottky barrier and thus a high-resistance contact is desirable to achieve a low dark current. This advantage will be elaborated more in the following sections when we address the photoresponse of the graphene–WSe$_2$–Au photodetector.
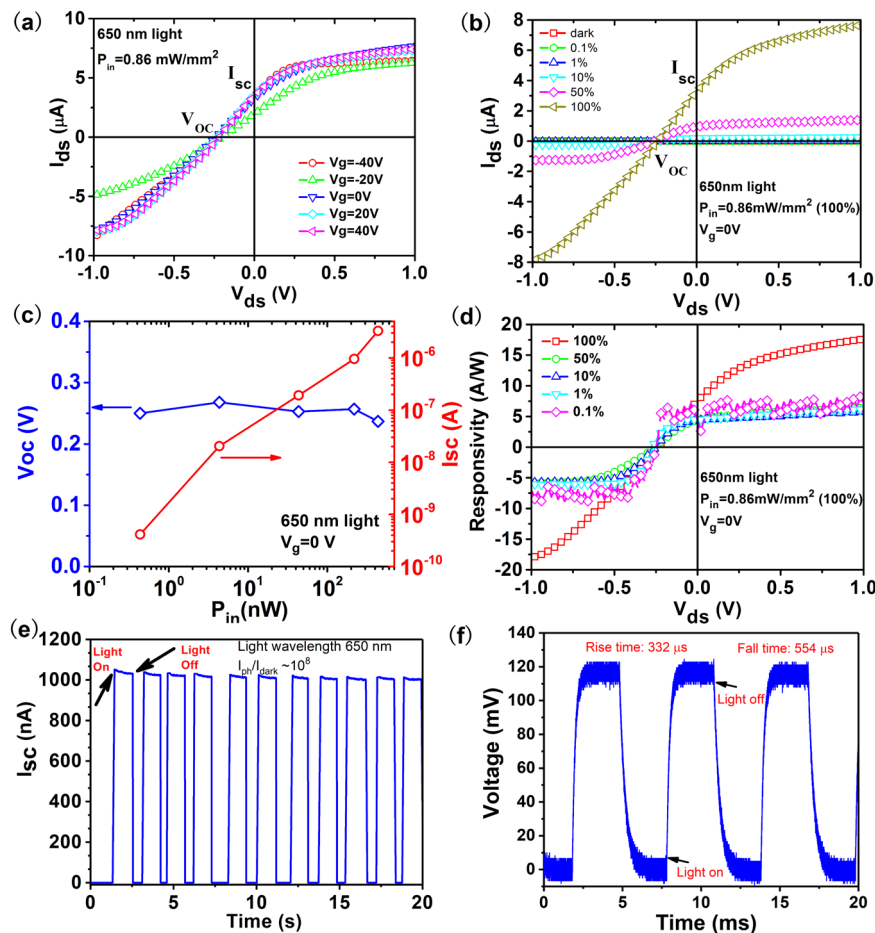
Fig. 3 Self-driven photoresponse of the photodetector. a Current–voltage (I–V) characteristics of the graphene–WSe$_2$–Au photodetector under different gate voltage bias. A 650-nm laser with the full power of 0.86 mW mm^{-2} is used as the light source. **b** I–V characteristics of the graphene–WSe$_2$–Au photodetector under varying light power densities and a zero gate voltage bias. **c** Dependence of I_{sc} and open-circuit voltage (V_{oc}) on the light power. **d** Dependence of the measured responsivity of the graphene–WSe$_2$–Au photodetector on the light power density. **e** Dynamic I_{sc} of the graphene–WSe$_2$–Au photodetector under a zero gate voltage bias. **f** Fall time and rise time of the photodetector extracted from the dynamic voltage exerted to the serial resistor.

Self-driven photoresponse characteristics

Figure 3a shows the current–voltage (I–V) curves of the graphene–WSe$_2$–Au MSM photodetector under the illumination of a 650 nm laser diode. During the photoresponse measurement, the photodetector is put on a probe station, and the laser light is illuminated on the whole device through a microscope mounted on top of the probe station. The light spot size is about 3 mm in diameter, and the full power of the 650 nm laser illuminated on the substrate is about 6.08 mW, which gives an equivalent power density of 0.86 mW mm^{-2}. The total light power illuminated on the photodetector is about 507.1 μm^2 × 0.86 mW mm^{-2} = 436 nW. The I–V curves show the clear photovoltaic effect of the photodetector. The measured photocurrent is in the range of −8.51 to 7.68 μA, which is at least four orders magnitude higher than the dark current shown in Fig. 2e in the measured V_{ds} range of −1 to 1 V. The self-driven characteristic is clearly identified by the large I_{sc} in Fig. 3a. The I_{sc} is about 3.29 μA under the zero gate bias condition, which corresponding to a responsivity of 7.55 A W^{-1}. Another feature of the self-driven characteristic is the open-circuit voltage V_{oc}, which is −0.24 V for the present photodetector. Figure 3b shows the I–V curves measured under varying light power density, and the dependence of I_{sc} and V_{oc} on the power density is summarized in Fig. 3c. It is noteworthy that the V_{oc} is almost a constant of ∼ −0.24 V over three orders of light power

density, and the I_{sc} exhibits a linear relationship with the light power density.

Figure 3d shows the responsivity calculated according to the equation[32]:

$$R = \frac{I_{ph}}{P_{in}} = \frac{I - I_{dark}}{P_{in}}, \qquad (5)$$

where I_{ph} is the photocurrent and is obtained by subtracting the dark current I_{dark} from the total current measured under light illumination, and P_{in} is the power density of the light. The responsivity obtained without any external bias, that is $V_{ds} = 0$ and $V_g = 0$, is almost invariant with the light power density in a dynamic range of 60 dB. The absolute value of the responsivity is about 4.38 A W^{-1} when the light power is in the range of 0.1–50% of the full light power, and it increases to 7.55 A W^{-1} when the light power increases to 100% of the full power. Even without any external bias, the responsivity is much larger than many 2D semiconductor based photodetectors operated with an external bias voltage[19,32]. Although the responsivity is not the highest among 2D materials based photodetectors, the high linearity over almost 60 dB is highly desirable for practical applications. In comparison, a typical silicon photodiode exhibits a responsivity <1 A W^{-1} in the visible light range, and features a linear relationship with the light power within a dynamic range of 40–60 dB[6]. We note that the responsivity of
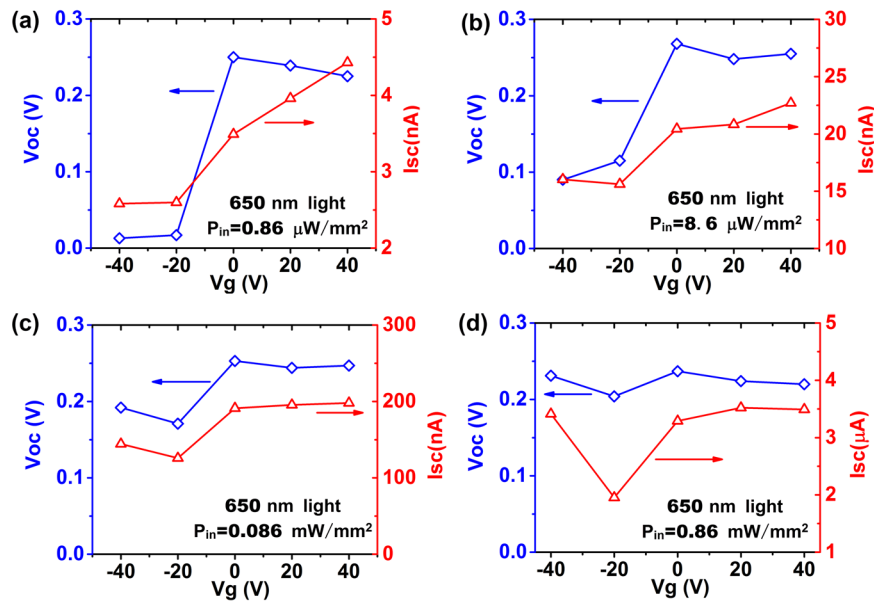
Fig. 4   Gate-tunable photoresponse. Dependence of the V_{oc} and I_{sc} on the gate voltage bias under 650 nm light illumination with a power density of a 0.86 μW mm^{-2}, **b** 8.6 μW mm^{-2}, **c** 0.086 mW mm^{-2}, and **d** 0.86 mW mm^{-2}.

the graphene–WSe$_2$–Au photodetector can be further increased by applying an external voltage bias V_{ds}, which changes the depletion width according to Eqs. (3) and (4) and causes an even larger asymmetry between the two MS junctions. Supplementary Figure 2 shows the I–V curves obtained with V_{ds} ranging from −3 to 3 V, from which the highest responsivity of ~25 A W^{-1} can be obtained.

Figure 3e shows the dynamic I_{sc} measured under the 650 nm light illumination. The gate voltage bias is also zero for dynamic measurement. When the light is off, the photodetector has a low dark current ~10^{-14} A. As the photocurrent is around 10^{-6} A, the photocurrent-to-dark current ratio, which is denoted as the I_{ph}/I_{dark} ratio in this paper, is larger than 10^8. Based on the acquired information about the self-driven photodetector, including the responsivity R (7.55 A W^{-1}), dark current I_{dark} (10^{-14} A), device area A (507.1 μm^2), the detectivity D* of the photodetector under zero bias can be estimated according to the equation[32]:

$$D^* = \frac{A^{1/2}R}{(2qI_{dark})^{1/2}},$$ (6)

which is about 3.0×10^{12} Jones and among the highest reported value for 2D material-based photodetectors[32]. By connecting the MSM photodetector to an external resistor, and measuring the dynamic voltage of the resistor with an oscilloscope, a rise time and fall time of 332 and 554 μs are extracted from the dynamic voltage signal waveform, respectively (Fig. 3f). The response time of the present device is still longer than some reported values, such as 15 μs for the CNT-MoS$_2$ heterojunction[33], and 30 μs for the Au–MoS$_2$–Au photodetector[34], which could be attributed to the larger channel length (~30 μm) than these devices (3.5 μm in ref. [34]). The response time could be further improved by optimizing the geometry of the devices (a shorter channel length), or eventually by adopting a vertical heterojunction that eliminates the lateral channel.

Scanning photocurrent measurement (SPCM) is widely applied to identify the sources of the photocurrent[34–36]. We have further performed SPCM on the same device. Supplementary Figure 3 shows SPCM image measured under a zero bias. The location of the highest photocurrent is at the Au–WSe$_2$ junction, which is due to the large Schottky barrier height between the high work function Au and the ambipolar WSe$_2$. As the depletion region

extends to the WSe$_2$ channel area, we could also observe the photocurrent in the WSe$_2$ layer, although the magnitude is relatively smaller than that at the junction. The assumption that the Au–WSe$_2$ junction and WSe$_2$–Gr junction has a different barrier height can be verified from the distinct photocurrent observed at the two junction regions.

Gate-tunable characteristics of the self-driven photodetector
For a traditional MSM photodetector based on bulk semiconductor materials, a thick substrate is required to obtain a high absorbance of the incoming light, and the device is a two-terminal device. In the present study, as the 2D material has a much higher absorption, a thin film is enough to absorb the incoming light, which makes it possible to add the third terminal to control the Fermi level of the 2D semiconductor, as well as the Schottky barrier of the MS junctions. This effect is experimentally verified and reported in Fig. 4. It is noteworthy that the absolute value of V_{oc} increases sharply from 0.02 to 0.25 V when the gate bias increases from −20 to 0 V, as shown in Fig. 4a. Referring to Fig. 2e, we note that the polarity of the carriers changes from the p-type to n-type when the gate bias increases from −20 to 0 V. For a p-type WSe$_2$ whose Fermi level is closer to the Au electrode, a small Au–WSe$_2$ barrier height is expected because of the high work function of Au. For the graphene–WSe$_2$ MS junction, the Fermi levels of both WSe$_2$ and graphene could be tuned by the applied gate bias; thus, the originally small barrier height does not change too much as the other MS junction. As a result, the difference of the barrier height of the two MS junctions is smaller for a negative gate voltage bias voltage. When the gate bias voltage is larger than −5 V, n-type transport is dominant and the Au–WSe$_2$ exhibits a larger barrier height, which results in a larger asymmetry between the two MS junctions.

Figure 4c, d shows that as the light power increases, the V_{oc} also increases for the negative gate bias region. For the largest power density of 0.86 mW mm^{-2} used in this study, the V_{oc} is almost independent of the applied gate voltage bias, which indicates that the photogenerated carrier concentration dominates over the gate bias induced carrier concentration. In that case, the Fermi level, or more precisely the quasi-Fermi level of WSe$_2$, is mainly controlled by photogenerated carriers, and the Schottky barriers
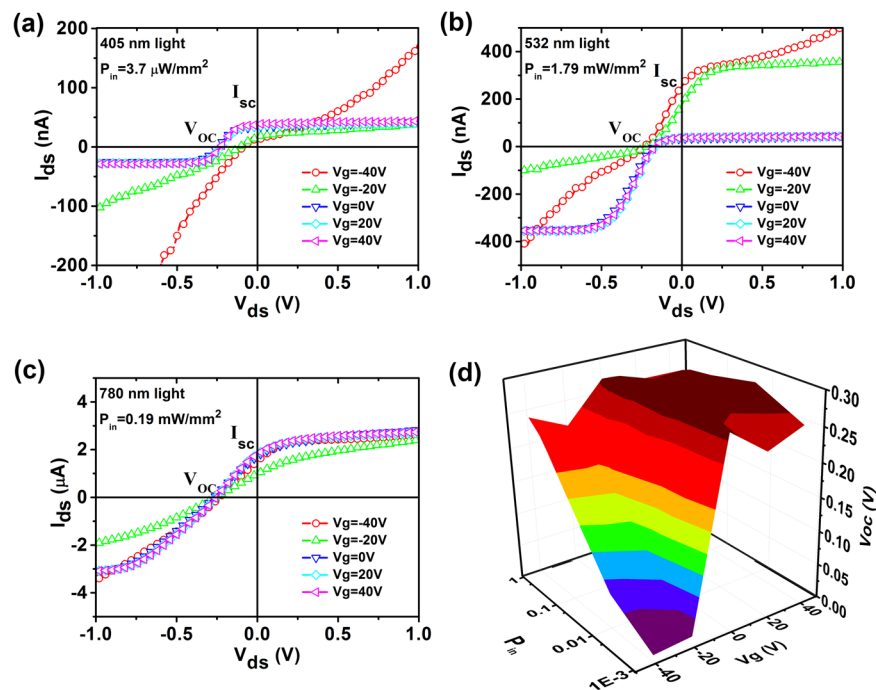
Fig. 5 Broadband photoresponse of the self-driven photodetector. I–V curves of the self-driven graphene–WSe_2–Au photodetector under varying light wavelengths of **a** 405 nm, **b** 532 nm, and **c** 780 nm. **d** Dependence of the V_{oc} on the gate voltage bias and light power density under 780 nm light illumination.

difference and V_{oc} is determined by the work function difference between graphene and Au electrodes. In accordance with the V_{oc}, the I_{sc} exhibits the same gate tunable and light power dependence characteristics.

We have also measured the transfer curves under illumination (650 nm, 100% intensity). Several phenomena could be observed from this measurement (Supplementary Fig. 4). Firstly, the photocurrent shows a constantly large value compared to the dark current. Secondly, for a relatively small V_{ds} (1–3 V), the photocurrent is almost a constant over the strong p-type (−40 to −20 V) and n-type (10–40 V) regions, suggesting the electric field is strong enough to separate the photogenerated carriers. Thirdly, in the transition region from the p-type to the n-type, a local minimum and maximum photocurrent is observed, which is due to the rapid change of the Fermi level of the WSe_2. Finally, we note that with a larger V_{ds} and V_g, the increasing photocurrent is probably due to the tunneling current assisted by the strong electric field in the heterojunction.

Broadband photoresponse of the self-driven photodetector

The broadband photoresponse of the self-driven photodetector is investigated in the wavelength range from 405 to 780 nm. The same self-driven characteristics, as indicated by the I_{sc} and V_{oc}, are observed for all the light wavelengths, as shown in Fig. 5. For the 405 nm light which has the full power of 3.7 μW mm^{-2}, an I_{sc} of 38.65 nA is recorded and the corresponding responsivity of 20.6 A W^{-1} is obtained (Fig. 5a). Gate-tunable V_{oc} and I_{sc} follow the same trend as reported for the 650 nm light illumination (Supplementary Fig. 5) with a similar power density. The largest V_{oc} of 0.295 V is obtained with a laser wavelength of 780 nm and a P_{in} of 1.9 μW mm^{-2} (Supplementary Fig. 6), while the highest zero-bias responsivity of 16.54 A W^{-1} is obtained under a P_{in} of 0.19 mW mm^{-2}, as shown in Fig. 5c, d summarizes the dependence of V_{oc} on the gate voltage bias and the power density of a 780 nm laser. In general, the V_{oc} shows the same gate-tunable effect as that analyzed for the photodetector under 650 nm light illumination.

Modeling and analysis of the self-driven photodetector

To get a deep understanding of the self-driven property of the graphene–WSe_2–Au photodetector, we have performed numerical simulation of the photodetector based on the finite element analysis method. A 2D structure is constructed with both graphene–WSe_2 and Au–WSe_2 MS junction modeled as an ideal Schottky contact (Supplementary Fig. 7). From previous experimental results, we note that the highest V_{oc} is obtained when the gate voltage is between −10 and 0 V, and the corresponding electric field-induced carrier concentration is below 2.16×10^{17} cm^{-3}. Figure 6a shows the simulated I–V curves of three different MSM photodetectors under 650 nm light illumination. The only difference of the MSM photo-detectors is the electrode configurations as shown in the legend in Fig. 6a. The work functions of the graphene and Au electrodes are chosen as 4.6 and 4.9 eV, respectively. While the three devices show almost the same saturated photocurrent at a large voltage bias, only the asymmetrical Gr–WSe_2–Au structure exhibits the photovoltaic effect. The dark current of the three photodetectors, which is at least three orders of magnitude that the photocurrent (Supplementary Fig. 8), can be neglected when analyzing its contribution to the total current of the photodetector under light illumination with a large power density. As a comparison, we have also fabricated symmetrical Au–WSe_2–Au photodetectors. The I–V curvers under illumination also shows symmetrical characteristics without any photovoltaic effect (Supplementary Fig. 9). As shown in Fig. 6b, the simulated V_{oc} increases with increasing light power, and the largest absolute value of V_{oc} is 0.3 V which is exactly the same as the barrier height difference between the two MS junctions. One origin of the relatively smaller V_{oc} under a small P_{in} is the dark current contribution from the reversed-biased Gr–WSe_2 junction, which is comparable to the photocurrent and effectively decreases the voltage bias needed to compensate the photocurrent difference from the two MS junctions. Figure 6c summarizes the dependence of V_{oc} and I_{sc} on the light power density. The high linearity of the I_{sc}
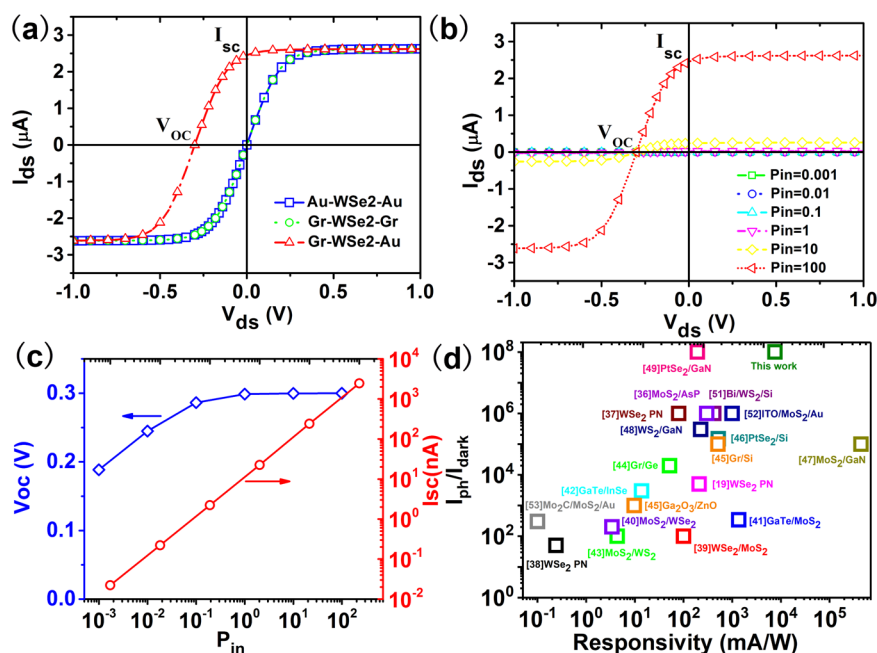
Fig. 6 **Theoretical analysis and performance comparison of the self-driven photodetector. a** Simulated $I–V$ curves of three MSM photodetectors with different electrode configurations. **b** Simulated $I–V$ curves of the Gr–WSe$_2$–Au photodetector under various light power densities. **c** Dependence of V_{oc} and I_{sc} on the light power density. **d** Comparison of the performances of self-driven photodetectors based on different materials and working mechanisms.

with light power can be obtained over at least five orders of magnitude of the light power, which is very beneficial for future practical applications.

Up to now, there are mainly three types of self-driven photodetectors based on 2D materials, including PN junctions built on the same material, PN junction by stacking two different semiconducting materials, and MSM photodetectors with asymmetrical device structures. In Fig. 6d, we compare the key parameters including responsivity and I_{ph}/I_{dark} of various self-driven photodetectors. These data points in Fig. 6d are extracted from recently reported self-driven photodetectors based on different materials and working mechanisms[19,36–53], and the detailed performance metrics are listed in Supplementary Table 1. In general, our device shows a relatively high responsivity, and the highest reported I_{ph}/I_{dark} ratio under a zero bias, which origins from the proposed asymmetrical device structure featuring both asymmetrical MS junctions for a high zero-bias photocurrent and an ultralow dark current.

In summary, an asymmetrical Gr–WSe$_2$–Au MSM device structure is proposed to realize the self-driven photodetector. With both of the constituent MS junctions formed by the dry-transfer method, van der Waals contacts are obtained between WSe$_2$ and the electrode materials, thus preventing the notorious Fermi-level pinning effect in 2D materials based photodetectors. As a result, a high responsivity of 7.55 A W^{-1} is obtained under zero external voltage bias. Combining the low dark current of $\sim 10^{-14}$ A, a high detectivity of 3×10^{12} Jones and a high I_{ph}/I_{dark} of 10^8 is obtained for the present device. Furthermore, a numerical simulation is performed to explain the device physics of the proposed device structure, including the self-driven property and its dependence on the light power density. The photodetector also exhibits high linearity with the light power density, which is very important for its implementation with processing circuits for practical low-power applications.

METHODS

Device fabrication

For device fabrication, a silicon wafer with a 100-nm-thick thermally grown SiO$_2$ was chosen as the starting substrate. We prepared the Au electrodes on top of the SiO$_2$/Si substrate by following the standard photolitho-graphy, Au/Ti (50 nm/10 nm) evaporation, and lift-off process flow. The WSe$_2$ flake with proper size is transferred to the PDMS stamp, which is then attached to a glass slide and aligned to the pattered Au electrode. For the first transfer process, a part of the chosen WSe$_2$ flake is coated on the Au electrode, while a large part of the WSe$_2$ flake is transferred onto the SiO$_2$/Si substrate. For the second transfer process, the graphene flake is aligned on top of the WSe$_2$ flake which is attached to the SiO$_2$/Si substrate. Part of the graphene flake is also contacted with another Au electrode for following electrical characterization.

Electrical and photoresponse characterizations

All the electrical and photoresponse measurements were conducted on a probe station connected to a semiconductor parameter analyzer Agilent 4156c. The laser is mounted on the microscope and the laser light is illuminated on the entire device through the lens of the microscope. The dynamic $I–V$ measurements were conducted using the same equipment by using the time sampling mode of 4156C. While the dynamic $I–V$ measurements could provide a high precision in measuring the ultralow dark current, the sampling speed is too low to extract the real response speed of the photodetector. By connecting the photo-detector to an external resistor (20 MΩ), and measuring the dynamic voltage of the resistor by an oscilloscope (Wavesurfer 510 1 GHz Oscilloscope), both the rise time and the fall time can be recorded with a higher speed. The photodetector is illuminated with a red-light laser diode powered by an external signal generator (Rigol DG4102). No external voltage is applied to the photodetector during the dynamic $I–V$ and voltage measurements.

DATA AVAILABILITY

The data supporting the findings of this work are available from the corresponding authors upon reasonable request.

REFERENCES

1. Fossum, E. R. & Hondongwa, D. B. A review of the pinned photodiode for CCD and CMOS image sensors. *IEEE J. Electron. Dev.* **2**, 33–43 (2014).
2. Assefa, S., Xia, F. & Vlasov, Y. A. Reinventing germanium avalanche photodetector for nanophotonic on-chip optical interconnects. *Nature* **464**, 80–84 (2010).
3. Bacon, C. P., Mattley, Y. & DeFrece, R. Miniature spectroscopic instrumentation: applications to biology and chemistry. *Rev. Sci. Instrum.* **75**, 1–16 (2004).
4. Shiraishi, K. et al. A 1.2e− temporal noise 3D-stacked CMOS image sensor with comparator-based multiple-sampling PGA. *ITE Tech. Rep.* **40**, 33–36.
5. Hirayama, T. The evolution of CMOS image sensors. In *2013 IEEE Asian Solid-State Circuits Conference (A-SSCC)*, Singapore 5–8.
6. El Gamal, A. & Eltoukhy, H. CMOS image sensors. *IEEE Circuits and Devices Magazine* Vol. 21, 6–20 (2005). https://doi.org/10.1109/MCD.2005.1438751.
7. Sze, S. M. & Ng, K. K. *Physics of Semiconductor Devices* (Wiley, 2006).
8. Muller, A. et al. GaN membrane metal-semiconductor-metal ultraviolet photodetector. *Appl. Opt.* **47**, 1453–1456 (2008).
9. Xu, H., Yin, L., Liu, C., Sheng, X. & Zhao, N. Recent advances in biointegrated optoelectronic devices. *Adv. Mater.* **30**, 1800156 (2018).
10. Nguyen, C. M. et al. Wireless sensor nodes for environmental monitoring in Internet of Things. In *2015 IEEE MTT-S International Microwave Symposium*, Phoenix, AZ, USA. 1–4.
11. Polat, E. O. et al. Flexible graphene photodetectors for wearable fitness monitoring. *Sci. Adv.* **5**, eaaw7846 (2019).
12. García de Arquer, F. P., Armin, A., Meredith, P. & Sargent, E. H. Solution-processed semiconductors for next-generation photodetectors. *Nat. Rev. Mater.* **2**, 16100 (2017).
13. Xia, F., Wang, H., Xiao, D., Dubey, M. & Ramasubramaniam, A. Two-dimensional material nanophotonics. *Nat. Photonics* **8**, 899–907 (2014).
14. Long, M., Wang, P., Fang, H. & Hu, W. Progress, challenges, and opportunities for 2D material based photodetectors. *Adv. Funct. Mater.* **29**, 1803807 (2018).
15. Pospischil, A. et al. CMOS-compatible graphene photodetector covering all optical communication bands. *Nat. Photonics* **7**, 892–896 (2013).
16. Zhang, W. et al. High-gain phototransistors based on a CVD MoS(2) monolayer. *Adv. Mater.* **25**, 3456–3461 (2013).
17. Lopez-Sanchez, O., Lembke, D., Kayci, M., Radenovic, A. & Kis, A. Ultrasensitive photodetectors based on monolayer MoS_2. *Nat. Nanotechnol.* **8**, 497–501 (2013).
18. Ko, S. et al. Few-layer WSe_2 Schottky junction-based photovoltaic devices through site-selective dual doping. *ACS Appl. Mater. Interfaces* **9**, 42912–42918 (2017).
19. Baugher, B. W., Churchill, H. O., Yang, Y. & Jarillo-Herrero, P. Optoelectronic devices based on electrically tunable p-n diodes in a monolayer dichalcogenide. *Nat. Nanotechnol.* **9**, 262–267 (2014).
20. Lee, C. H. et al. Atomically thin p-n junctions with van der Waals heterointerfaces. *Nat. Nanotechnol.* **9**, 676–681 (2014).
21. Mak, K. F. & Shan, J. Photonics and optoelectronics of 2D semiconductor transition metal dichalcogenides. *Nat. Photonics* **10**, 216–226 (2016).
22. Wang, Z. L. Self-powered nanosensors and nanosystems. *Adv. Mater.* **24**, 280–285 (2012).
23. Qiao, H. et al. Self-powered photodetectors based on 2D materials. *Adv. Opt. Mater.* **8**, 1900765 (2019).
24. Konstantatos, G. Current status and technological prospect of photodetectors based on two-dimensional materials. *Nat. Commun.* **9**, 5266 (2018).
25. Rogalski, A., Kopytko, M. & Martyniuk, P. Two-dimensional infrared and terahertz detectors: outlook and status. *Appl. Phys. Rev.* **6**, 021316 (2019).
26. McDonnell, S. et al. Hole contacts on transition metal dichalcogenides: interface chemistry and band alignments. *ACS Nano* **8**, 6265–6272 (2014).
27. Liu, Y. et al. Approaching the Schottky-Mott limit in van der Waals metal-semiconductor junctions. *Nature* **557**, 696–700 (2018).
28. Kim, K. et al. Band alignment in WSe_2-graphene heterostructures. *ACS Nano* **9**, 4527–4532 (2015).
29. Fang, H. et al. Strong interlayer coupling in van der Waals heterostructures built from single-layer chalcogenides. *Proc. Natl Acad. Sci. USA* **111**, 6198–6202 (2014).
30. Lee, I. et al. Gate-tunable hole and electron carrier transport in atomically thin dual-channel WSe_2/MoS_2 heterostructure for ambipolar field-effect transistors. *Adv. Mat.* **28**, 9519–9525 (2016).
31. Peng, B. et al. Ultrafast charge transfer in MoS_2/WSe_2 p–n Heterojunction. *2D Mater.* **3**, 025020 (2016).
32. Xie, C., Mak, C., Tao, X. & Yan, F. Photodetectors based on two-dimensional layered materials beyond graphene. *Adv. Funct. Mater.* **27**, 1603886 (2017).
33. Jariwala, D. et al. Gate-tunable carbon nanotube-MoS_2 heterojunction p-n diode. *Proc. Natl Acad. Sci. USA* **110**, 18076–18080 (2013).
34. Wu, C.-C. et al. Elucidating the photoresponse of ultrathin MoS_2 field-effect transistors by scanning photocurrent microscopy. *J. Phys. Chem. Lett.* **4**, 2508–2513 (2013).
35. Miao, J. et al. Gate-tunable semiconductor heterojunctions from 2D/3D van der Waals interfaces. *Nano Let.* **20**, 2907–2915 (2020).
36. Wu, F. et al. High efficiency and fast van der Waals hetero-photodiodes with a unilateral depletion region. *Nat. Commun.* **10**, 4663 (2019).
37. Tang, Y. et al. WSe_2 photovoltaic device based on intramolecular p-n junction. *Small* **15**, e1805545 (2019).
38. Groenendijk, D. J. et al. Photovoltaic and photothermoelectric effect in a double-gated WSe_2 device. *Nano Lett.* **14**, 5846–5852 (2014).
39. Deng, W. et al. High-performance photodiode based on atomically thin WSe_2/MoS_2 nanoscroll integration. *Small* **15**, e1901544 (2019).
40. Lin, P. et al. Piezo-phototronic effect for enhanced flexible MoS_2/WSe_2 van der Waals photodiodes. *Adv. Funct. Mater.* **28**, 1802849 (2018).
41. Yang, S. et al. Self-driven photodetector and ambipolar transistor in atomically thin $GaTe-MoS_2$ p-n vdW heterostructure. *ACS Appl Mater. Interfaces* **8**, 2533–2539 (2016).
42. Feng, W. et al. A fast and zero-biased photodetector based on $GaTe–InSe$ vertical 2D p–n heterojunction. *2D Mater.* **5**, 025008 (2018).
43. Wu, W. et al. Self-powered photovoltaic photodetector established on lateral monolayer MoS_2-WS_2 heterostructures. *Nano Energy* **51**, 45–53 (2018).
44. Zeng, L. H. et al. Monolayer graphene/germanium Schottky junction as high-performance self-driven infrared light photodetector. *ACS Appl Mater. Interfaces* **5**, 9362–9366 (2013).
45. Periyanagounder, D., Gnanasekar, P., Varadhan, P., He, J.-H. & Kulandaivel, J. High performance, self-powered photodetectors based on a graphene/silicon Schottky junction diode. *J. Mater. Chem. C* **6**, 9545–9551 (2018).
46. Xie, C. et al. High-performance broadband heterojunction photodetectors based on multilayered PtSe2 directly grown on a Si substrate. *Nanoscale* **10**, 15285–15293 (2018).
47. Liu, X. et al. Enhancing photoresponsivity of self-aligned MoS_2 field-effect transistors by piezo-phototronic effect from GaN nanowires. *ACS Nano* **10**, 7451–7457 (2016).
48. Zhao, Z. et al. Synthesis of large-area 2D WS_2 films and fabrication of a heterostructure for self-powered ultraviolet photodetection and imaging applications. *J. Mater. Chem. C* **7**, 12121–12126 (2019).
49. Zhuo, R. et al. In-situ fabrication of PtSe2/GaN heterojunction for self-powered deep ultraviolet photodetector with ultrahigh current on/off ratio and detectivity. *Nano Res.* **12**, 183–189 (2018).
50. Zhao, B. et al. An ultrahigh responsivity (9.7 mA W^{-1}) self-powered solar-blind photodetector based on individual $ZnO–Ga_2O_3$ heterostructures. *Adv. Funct. Mater.* **27**, 1700264 (2017).
51. Yao, J., Zheng, Z., Shao, J. & Yang, G. Promoting photosensitivity and detectivity of the Bi/Si heterojunction photodetector by inserting a WS2 Layer. *ACS Appl. Mater. Interfaces* **7**, 26701–26708 (2015).
52. Gong, F. et al. Visible to near-infrared photodetectors based on MoS_2 vertical Schottky junctions. *Nanotechnology* **28**, 484002 (2017).
53. Kang, Z. et al. MoS_2-based photodetectors powered by asymmetric contact structure with large work function difference. *Nano-Micro Lett.* **11**, 34 (2019).

ACKNOWLEDGEMENTS

AUTHOR CONTRIBUTIONS

C.Z. and Z.F. conceived and designed the research. S.Z., Z.L., and C.Y. prepared the sample and device. S.Z. and Z.M. conducted the electrical measurement and optical characterization of the fabricated devices. C.Z. performed the modeling of the photodetector and supervised the project. C.Z., S.Z., and M.C. co-wrote the manuscript, and all authors discussed the results and commented on the paper.

COMPETING INTERESTS

The authors declare no competing interests.

ADDITIONAL INFORMATION